



**HAL**  
open science

# Segmentation of skin lesions in 2D and 3D ultrasound images using a spatially coherent generalized Rayleigh mixture model

Marcelo Alejandro Pereyra, Nicolas Dobigeon, Hadj Batatia, Jean-Yves Tourneret

► **To cite this version:**

Marcelo Alejandro Pereyra, Nicolas Dobigeon, Hadj Batatia, Jean-Yves Tourneret. Segmentation of skin lesions in 2D and 3D ultrasound images using a spatially coherent generalized Rayleigh mixture model. IEEE Transactions on Medical Imaging, 2012, 31 (8), pp.1509-1520. 10.1109/TMI.2012.2190617 . hal-03531032

**HAL Id: hal-03531032**

**<https://hal.science/hal-03531032v1>**

Submitted on 18 Jan 2022

**HAL** is a multi-disciplinary open access archive for the deposit and dissemination of scientific research documents, whether they are published or not. The documents may come from teaching and research institutions in France or abroad, or from public or private research centers.

L'archive ouverte pluridisciplinaire **HAL**, est destinée au dépôt et à la diffusion de documents scientifiques de niveau recherche, publiés ou non, émanant des établissements d'enseignement et de recherche français ou étrangers, des laboratoires publics ou privés.



## Open Archive TOULOUSE Archive Ouverte (OATAO)

OATAO is an open access repository that collects the work of Toulouse researchers and makes it freely available over the web where possible.

This is an author-deposited version published in : <http://oatao.univ-toulouse.fr/>  
Eprints ID : 6276

To link to this article :

URL : <http://ieeexplore.ieee.org/xpl/articleDetails.jsp?arnumber=6168272>

<p>To cite this version : Pereyra, Marcelo and Dobigeon, Nicolas and Batatia, Hadj and Tournet, Jean-Yves <i>Segmentation of skin lesions in 2D and 3D ultrasound images using a spatially coherent generalized Rayleigh mixture model</i>. (2012) IEEE Transactions on Medical Imaging, vol. 31 (n° 8). pp. 1509-1520. ISSN 0278-0062</p>
--

Any correspondence concerning this service should be sent to the repository administrator: [staff-oatao@listes.diff.inp-toulouse.fr](mailto:staff-oatao@listes.diff.inp-toulouse.fr)

# Segmentation of Skin Lesions in 2-D and 3-D Ultrasound Images Using a Spatially Coherent Generalized Rayleigh Mixture Model

Marcelo Pereyra\*, Nicolas Dobigeon, Hadj Batatia, and Jean-Yves Tournet

**Abstract**—This paper addresses the problem of jointly estimating the statistical distribution and segmenting lesions in multiple-tissue high-frequency skin ultrasound images. The distribution of multiple-tissue images is modeled as a spatially coherent finite mixture of heavy-tailed Rayleigh distributions. Spatial coherence inherent to biological tissues is modeled by enforcing local dependence between the mixture components. An original Bayesian algorithm combined with a Markov chain Monte Carlo method is then proposed to jointly estimate the mixture parameters and a label-vector associating each voxel to a tissue. More precisely, a hybrid Metropolis-within-Gibbs sampler is used to draw samples that are asymptotically distributed according to the posterior distribution of the Bayesian model. The Bayesian estimators of the model parameters are then computed from the generated samples. Simulation results are conducted on synthetic data to illustrate the performance of the proposed estimation strategy. The method is then successfully applied to the segmentation of *in vivo* skin tumors in high-frequency 2-D and 3-D ultrasound images.

**Index Terms**—Bayesian estimation, Gibbs sampler, heavy-tailed Rayleigh distribution, mixture model, Potts–Markov field.

## I. INTRODUCTION

ULTRASOUND imaging is a longstanding medical imaging modality with important applications in diagnosis, preventive examinations, therapy and image-guided surgery. In dermatologic oncology, diagnosis relies mainly on surface indicators such as color, shape, and texture whereas the two more reliable measures are the depth of the lesion and the number of skin layers that have been invaded. Currently, these can only be evaluated after excision. Recent advances in high-frequency transducers and 3-D probes have opened new opportunities to perform noninvasive diagnostics using ultrasound images. However, changing dermatological practices requires developing robust segmentation algorithms. Despite the extensive literature on the subject, accurate segmentation

of ultrasound images is still a challenging task and a focus of considerable research efforts. Current segmentation techniques are extremely application-specific, developed mainly for echocardiography followed by transrectal prostate examination (TRUS), kidney, breast cancer and (intra) vascular diseases (IVUS) [3]. A survey of the state-of-the-art methods up to 2006 is presented in [3].

Segmentation in echocardiography, TRUS and IVUS is mainly concerned with the detection and tracking of organ boundaries. Lesion delimitation is significantly different and more challenging. On one hand, unlike organs, lesions exhibit soft or “fuzzy” edges that are difficult to capture with boundary detection techniques. On the other, their echogenic and statistical characteristics are visibly different from those of their surrounding tissues. This fact has motivated the development of region-based segmentation techniques as opposed to boundary-based methods, which are still an active research subject in other medical ultrasound domains [4]–[6]. Similarly, lesions do not have anatomically predefined shapes as is the case for organs and are unlikely to benefit in the near future from recent works on anatomical or learned statistical shape priors [7]–[9]. This might change with the improvement of geometric tumor growth models derived from computational biology [10]. Early lesion segmentation methods have focused mainly on thresholding [11], [12] and were superseded by texture-based techniques. Madabhushi *et al.* derived an active contour based on texture and boundary features [13]. Huang *et al.* proposed a texture segmentation technique based on a neural network and a watershed algorithm [14]. In addition, Gaussian mixture models coupled with Markov random fields were proposed to segment lesions based on their region statistics [15], [16]. Moreover, since the important work of Dias *et al.* [17], Rayleigh mixtures have become a powerful model for region-based ultrasound image segmentation. The use of Rayleigh instead of Gaussian distributions is strongly justified by the physics of the image formation process that generates B-mode ultrasound images [18]. Based on the assumption that each biological tissue has its proper Rayleigh statistics, tissue segmentation is achieved by separating the mixture components. This is achieved by finding the maximum-likelihood (ML) or maximum-a-posteriori (MAP) estimators of the lesion contours. The optimization problem stemming from the ML and MAP estimators was solved in [17] using an interactive dynamic programming algorithm that jointly estimated the MAP contour and the mixture parameters. The authors performed several experiments on real echocardiography images and showed that the proposed method accurately segments heart walls.

\*M. Pereyra is with the University of Toulouse, IRIT/INP-ENSEEIH, 31071 Toulouse Cedex 7, France (e-mail: marcelo.pereyra@enseeiht.fr).

N. Dobigeon, H. Batatia, and J.-Y. Tournet are with the University of Toulouse, IRIT/INP-ENSEEIH, 31071 Toulouse Cedex 7, France (e-mail: nicolas.dobigeon@enseeiht.fr; hadj.batatia@enseeiht.fr; jean-yves.tournet@enseeiht.fr).

With the development of deformable models, Brusseau *et al.* proposed a statistical parametric active contour (AC) [19]. A parametric AC is a regularized curve defined by a set of points in the image domain that can be moved to maximize the segmentation posterior [20]. In the work of Brusseau *et al.*, the two-mixture components were separated using a statistical region AC which iteratively estimated the Rayleigh parameter of each component and evolved to optimize the segmentation. Also, given that convergence to a global optimum is not guaranteed, the authors proposed an *ad-hoc* automatic initialization technique. This method was further improved by Cardinal *et al.* [21] who substituted the parametric AC by an edge-based level set (LS) derived from the original work of Osher and Sethian [22]. A second modification was the introduction of an expectation-maximization (EM) algorithm to estimate the mixture parameters during initialization, thus removing the need to estimating them iteratively. The authors reported that the Rayleigh mixture LS method outperforms classical gradient-based LS at intravascular image segmentation. In addition, Saroul *et al.* recently applied the Rayleigh mixture model to prostate segmentation in transrectal ultrasound images [23]. In this case, the LS was replaced by a deformable model based on a super ellipse whose evolution was computed using a variational algorithm. The authors showed that the regularization introduced by this deformable model could compensate partial occlusion.

Rayleigh-mixture models were extended to tissues with generalized Rayleigh statistics by Destremes *et al.* [24], who proposed a carotid artery segmentation method based on a Nakagami mixture and a deformable model. As in [21], the estimation of the mixture parameters was achieved using an EM algorithm under the assumption that observations are independent. The evolution of the deformable model was computed using exploration/selection, a stochastic optimization algorithm that converges to the global optimum. However, since the mixture parameters are estimated with an EM algorithm, overall global convergence is not guaranteed. One other important contribution is the Rayleigh region-based LS method presented in [25], that adapted the fundamental work of Chan and Vese [26] on ACs without edges to ultrasound images with Rayleigh statistics. These region-based LS should be very appropriate for ultrasound images of lesions as they are able to segment objects with smooth edges under poor signal-to-noise ratio conditions. This work was recently generalized to all the distributions from the exponential family (i.e., Gamma, Rayleigh, Poisson, etc.) in [27]. However, these methods have not yet been applied to lesion segmentation in ultrasound images.

This paper addresses the problem of jointly estimating the statistical distribution and segmenting lesions in multiple-tissue 2-D and 3-D high-frequency skin ultrasound images. To our knowledge this is the first ultrasound image segmentation method specific to skin lesions. We propose to model multiple-tissue images using a heavy-tailed Rayleigh mixture, a model that has been inspired by the single-tissue model studied in [28]. The proposed mixture model is equipped with a Markov random field (MRF) that takes into account the spatial correlation inherent to biological tissues. Note that Potts Markov fields are particularly well suited for label-based segmentation as explained in [29] and further studied in [30]–[33]. Potts Markov models enhance segmentation because of their ability to capture the spatial correlation that exists between neighbor class labels

[30]. This correlation arises naturally from the spatial organization of biological tissues and is particularly important in skin because of its layered structure. Finally, while the Potts prior is an effective means to introduce spatial correlation between the class labels, it is interesting to mention that other more complex models could have been used instead. In particular, Marroquin *et al.* [34] have shown that better segmentation results may be obtained by using a two-layer hidden field, where hidden labels are assumed to be independent and correlation is introduced at a deeper layer by a vectorial Markov field. Similarly, Woolrich *et al.* [35] have proposed to approximate the Potts field by modeling mixture weights with a Gauss–Markov random field. However, these alternative models are not well adapted for 3-D images because they require significantly more computation complexity and memory resources than the Potts model. These overheads result from the fact that they introduce  $(K + 1)N$  and  $KN$  hidden variables, respectively, against only  $N$  for the Potts model ( $N$  being the number of voxels and  $K$  the number of classes). In addition, the segmentation problem is solved using a stochastic optimization algorithm with guaranteed global convergence, removing the need for an initial contour or supervised training. The paper is organized as follows. The statistical model used for an ultrasound image voxel is introduced in Section II. Section III introduces the Bayesian model used for the segmentation of ultrasound images. A hybrid Gibbs sampler generating samples asymptotically distributed according to the posterior distribution of this Bayesian model is described in Section IV. Experiments on synthetic and real data are presented in Section V. Conclusions are finally reported in Section VI.

## II. PROBLEM STATEMENT

This section describes the mixture model used for ultrasound image voxels. Let  $r_n \in \mathbb{R}^+$  denote an observation, or voxel, in an envelope (B-mode) ultrasound image  $\mathbf{r} = (r_1, \dots, r_N)^T$  without logarithmic compression. We assume that  $r_n$  is defined by means of the widely accepted point scattering model [36]

$$r_n = \left| \sum_{i=1}^M a_i [p(t_n - \tau_i) + j\tilde{p}(t_n - \tau_i)] \right| \quad (1)$$

where  $M$  is the total number of punctual scatterers,  $p(t) + j\tilde{p}(t)$  denotes the analytic extension of the interrogating pulse  $p(t)$ ,  $a_i \in (0, 1)$  is the cross-section of the  $i$ th scatterer,  $\tau_i \in \mathbb{R}^+$  is the time of arrival of the  $i$ th backscattered wave and  $t_n$  is the sampling time associated with  $r_n$ . Recent works on scattering in biological tissues have established that  $r_n$ , as defined above, converges in distribution towards an  $\alpha$ -Rayleigh distribution as  $M$  increases [28]

$$r_n \xrightarrow[M \rightarrow \infty]{d} \alpha \mathcal{R}(\alpha_n, \gamma_n) \quad (2)$$

where  $\xrightarrow[M \rightarrow \infty]{d}$  denotes convergence in distribution, the parameters  $\alpha_n \in (0, 2]$  and  $\gamma_n \in \mathbb{R}^+$  are the characteristic index and spread associated with the  $n$ th voxel.

This paper considers the case where the ultrasound image  $\mathbf{r}$  is made up by multiple biological tissues with high scatter density (i.e.,  $M \rightarrow \infty$ ), each with its own echogenicity and therefore its proper speckle statistics. In view of this spatial configuration,

we propose to model  $\mathbf{r}$  by an  $\alpha$ -Rayleigh stationary process with piecewise constant parameters. More precisely, we assume that there is a set of stationary classes  $\{C_1, \dots, C_K\}$  such that

$$\forall r_n \in C_k, \quad r_n \sim \alpha\mathcal{R}(\alpha_k, \gamma_k) \quad (3)$$

where  $\alpha_k$  and  $\gamma_k$  are the parameters associated with the class  $C_k$  (i.e., the  $k$ th biological tissue). As a consequence, it is possible to express the distribution of  $r_n$  by means of the following mixture of  $\alpha$ -Rayleigh distributions

$$r_n \sim \sum_{k=1}^K \omega_k \alpha\mathcal{R}(\alpha_k, \gamma_k) \quad (4)$$

where  $K$  is the number of classes and  $\omega_k$  represents the relative weight (or proportion) of the  $k$ th class with  $\sum_k \omega_k = 1$ . Lastly, to take into account the spatial coherence inherent to biological tissues we will consider that the class of a given voxel depends on those of its neighbors.

It should be noted that the proposed  $\alpha$ -Rayleigh mixture model is closely related to two other mixture models. On the one hand it generalizes the Rayleigh mixture model, which has been extensively applied to ultrasound image modeling. On the other, it can be shown that before being transformed by acquisition and demodulation, radio-frequency ultrasound signals are distributed according to a symmetric  $\alpha$ -stable distribution [28]. Hence, the proposed  $\alpha$ -Rayleigh mixture model can be interpreted as a transformation of the symmetric  $\alpha$ -stable mixture model studied in [37]. In addition, it is interesting to mention that the  $\alpha$ -Rayleigh distribution has been used successfully for SAR images in [38] and [39]. The methods proposed in [38] and [39] have been recently applied to characterize tissues in annotated ultrasound images [28]. This paper extends those methods by including in the estimation problem the identification of regions in the image with similar  $\alpha$ -Rayleigh parameters (each region being associated with a different tissue). This is achieved by proposing a novel Bayesian estimation algorithm based on the  $\alpha$ -Rayleigh mixture model (4) coupled with an MRF prior that captures the spatial coherence inherent to biological tissues. Finally, akin to [19], [21], [24], [25], note that the model (4) uses a simplified image representation based on regions and does not describe the boundaries between tissues explicitly.

The following section addresses the problem of estimating the parameters of the spatially coherent  $\alpha$ -Rayleigh mixture model introduced in (4) and performing the segmentation of ultrasound images.

### III. BAYESIAN MODEL

A label vector  $\mathbf{z} = (z_1, \dots, z_N)^T$  is introduced to map observations  $\mathbf{r}$  to classes  $C_1, \dots, C_K$  (i.e.,  $z_n = k$  if and only if  $r_n \in C_k$ ). This label vector will allow each image observation to be characterized and different kinds of tissues to be discriminated. Note that the weights  $\omega_k$  are directly related to the labels through the probabilities  $P[z_n = k] = \omega_k$  for  $k = 1, \dots, K$ . Consequently, the unknown parameter vector for the mixture (4) can be defined as  $(\boldsymbol{\theta}, \mathbf{z})$  where  $\boldsymbol{\theta} = (\boldsymbol{\alpha}^T, \boldsymbol{\gamma}^T)^T$  with  $\boldsymbol{\alpha} = (\alpha_1, \dots, \alpha_K)^T$  and  $\boldsymbol{\gamma} = (\gamma_1, \dots, \gamma_K)^T$ . This section

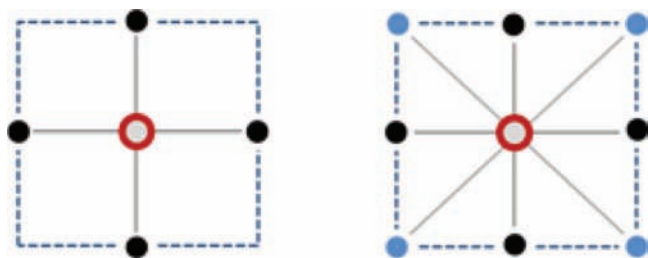


Fig. 1. Four-pixel (left) and eight-pixel (right) neighborhood structures. The pixel considered appears as a void red circle whereas its neighbors are depicted in full black and blue.

studies a Bayesian model associated with  $(\boldsymbol{\theta}, \mathbf{z})$ . This model requires defining the likelihood and the priors for the unknown parameters.

#### A. Likelihood

Assuming that the observations  $r_n$  are independent and using the mixture model (4), the likelihood of the proposed Bayesian model can be written as

$$p(\mathbf{r}|\boldsymbol{\theta}, \mathbf{z}) = \prod_{k=1}^K \prod_{\{n|z_n=k\}} p_{\alpha\mathcal{R}}(r_n|\alpha_k, \gamma_k) \quad (5)$$

where  $\{n|z_n = k\}$  denotes the subset of indexes  $n = 1, \dots, N$  that verify  $z_n = k$  and

$$p_{\alpha\mathcal{R}}(r_n|\alpha_k, \gamma_k) = r_n \int_0^\infty \lambda \exp[-(\gamma_k \lambda)^{\alpha_k}] J_0(r_n \lambda) d\lambda \quad (6)$$

is the probability density function (pdf) of an  $\alpha$ -Rayleigh distribution with parameters  $\alpha_k$  and  $\gamma_k$  and  $J_0$  is the zeroth-order Bessel function of the first kind.

#### B. Parameter Priors

1) *Labels*: It is natural to consider that there is some correlation between the probabilities  $P[z_n = k]$  of a given voxel and those of its neighbors. Since the seminal work of Geman [40], MRFs have become very popular to model neighbor correlation in images. MRFs assume that the distribution of a pixel conditionally to all other pixels of the image equals the distribution of this pixel conditionally to its neighbors. Consequently, it is important to properly define the neighborhood structure. The neighborhood relation between two pixels (or voxels)  $i$  and  $j$  has to be symmetric: if  $i$  is a neighbor of  $j$  then  $j$  is also a neighbor of  $i$ . There are several neighborhood structures that have been used in the literature. In the bidimensional case, neighborhoods defined by the four or eight nearest voxels represented in Fig. 1 are the most commonly used. Similarly, in the tridimensional case the most frequently used neighborhoods are defined by the six or fourteen nearest voxels represented in Fig. 2. In the rest of this paper four-pixel neighborhoods will be considered for 2-D images and six-voxel neighborhoods for 3-D images. Therefore, the associated set of neighbors, or cliques, can only have vertical, horizontal and depth configurations (see [40] and [41] for more details).

Once the neighborhood structure has been established, the MRF can be defined. Let  $z_n$  denote the random variable indicating the class of the  $n$ th image voxel. In the case

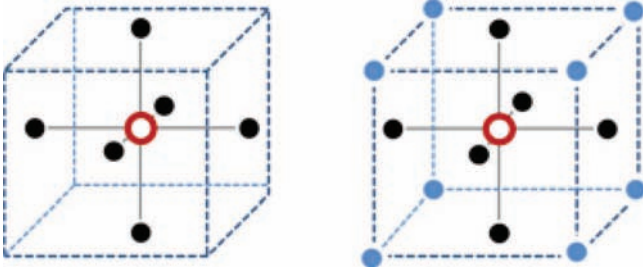


Fig. 2. Six-voxel (left) and fourteen-voxel (right) neighborhood structures. The voxel considered appears as a void red circle whereas its neighbors are depicted in full black and blue.

of  $K$  classes, the random variables  $z_1, \dots, z_N$  take their values in the finite set  $\{1, \dots, K\}$ . The whole set of random variables  $\mathbf{z}$  forms a random field. An MRF is then defined when the conditional distribution of  $z_n$  given the other pixels  $\mathbf{z}_{-n} = (z_1, \dots, z_{n-1}, z_{n+1}, \dots, z_N)$  only depends on its neighbors  $\mathbf{z}_{\mathcal{V}(n)}$ , i.e.,

$$P[z_n | \mathbf{z}_{-n}] = P[z_n | \mathbf{z}_{\mathcal{V}(n)}] \quad (7)$$

where  $\mathcal{V}(n)$  contains the neighbors of  $z_n$  according to the neighborhood structure considered.

In this study, we will first consider 2-D and 3-D Potts Markov fields as prior distributions for  $\mathbf{z}$ . More precisely, 2-D MRFs are considered for single-slice (2-D) ultrasound images whereas 3-D MRFs are used for multiple-slice (3-D) images. In light of the Hammersley–Clifford theorem, the corresponding prior for  $\mathbf{z}$  can be expressed as follows:

$$p(\mathbf{z}) = \frac{1}{C(\beta)} \exp \left[ \sum_{n=1}^N \sum_{n' \in \mathcal{V}(n)} \beta \delta(z_n - z_{n'}) \right] \quad (8)$$

where  $\beta$  is the granularity coefficient,  $C(\beta)$  is the normalizing constant or partition function [42] and  $\delta(\cdot)$  is the Kronecker function. The hyperparameter  $\beta$  tunes the degree of homogeneity of each region in the image. A small value of  $\beta$  induces a noisy image with a large number of regions, contrary to a large value of  $\beta$  that leads to few and large homogeneous regions. In this work, the granularity coefficient  $\beta$  will be fixed *a priori*. However, it is interesting to mention that the estimation of  $\beta$  has been receiving a lot of attention in the literature [33], [43]–[46]. Estimating the granularity coefficient using one of these methods is clearly an interesting problem that will be investigated in future work. Finally, it is interesting to note that despite not knowing  $C(\beta)$ , drawing labels  $\mathbf{z} = (z_1, \dots, z_N)$  from the distribution (8) can be easily achieved by using a Gibbs sampler [47].

2)  *$\alpha$ -Rayleigh Parameters*: The prior for each characteristic index  $\alpha_k$  ( $k = 1, \dots, K$ ) is a uniform distribution on  $(0, 2]$

$$\alpha_k \sim \mathcal{U}(0, 2). \quad (9)$$

This choice is motivated by the fact that the only information available *a priori* about this parameter, is that it can take values in the interval  $(0, 2]$ .

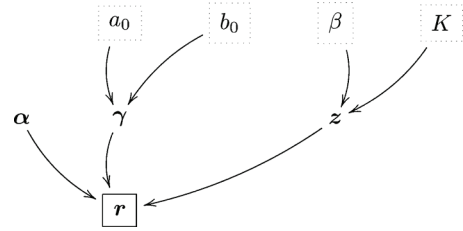


Fig. 3. DAG for the  $\alpha$ -Rayleigh mixture model (the fixed nonrandom hyperparameters appear in dashed boxes).

The prior for each spread parameter  $\gamma_k$  is an inverse gamma distribution with hyperparameters  $a_0$  and  $b_0$

$$\gamma_k \sim \mathcal{IG}(a_0, b_0), \quad k = 1, \dots, K. \quad (10)$$

This choice is motivated by the fact that the inverse gamma distribution allows either very vague or more specific prior information to be incorporated depending on the choice of the hyperparameters  $a_0$  and  $b_0$  ( $a_0 = b_0 = 1$  will be used in our experiments corresponding to a vague prior distribution).

Assuming *a priori* independence between the parameters  $\alpha_k$  and  $\gamma_k$ , the prior for  $\boldsymbol{\theta}$  is

$$p(\boldsymbol{\theta}) = p(\boldsymbol{\alpha})p(\boldsymbol{\gamma}) = \prod_{k=1}^K p(\alpha_k)p(\gamma_k). \quad (11)$$

We will also assume that the  $\alpha$ -Rayleigh parameters are independent from the labels associated with the image voxels. Thus the joint prior for the unknown parameters  $(\boldsymbol{\theta}, \mathbf{z})$  can be expressed as

$$p(\boldsymbol{\theta}, \mathbf{z}) = p(\mathbf{z})p(\boldsymbol{\theta}) \quad (12)$$

where  $p(\mathbf{z})$  has been defined in (8) and  $p(\boldsymbol{\theta})$  in (11).

Fig. 3 presents the proposed Bayesian model as a directed acyclic graph (DAG) summarizing the relationships between the different parameters and hyperparameters.

### C. Posterior Distribution of $(\boldsymbol{\theta}, \mathbf{z})$

Using Bayes theorem, the posterior distribution of  $(\boldsymbol{\theta}, \mathbf{z}) = (\boldsymbol{\alpha}, \boldsymbol{\gamma}, \mathbf{z})$  can be expressed as follows:

$$p(\boldsymbol{\theta}, \mathbf{z} | \mathbf{r}) = \frac{p(\mathbf{r} | \boldsymbol{\theta}, \mathbf{z})p(\boldsymbol{\theta}, \mathbf{z})}{p(\mathbf{r})} \propto p(\mathbf{r} | \boldsymbol{\theta}, \mathbf{z})p(\boldsymbol{\theta}, \mathbf{z}) \quad (13)$$

where  $\propto$  means “proportional to” and the likelihood  $p(\mathbf{r} | \boldsymbol{\theta}, \mathbf{z})$  and the joint prior  $p(\boldsymbol{\theta}, \mathbf{z})$  have been defined in (5) and (12).

Unfortunately, the posterior distribution (13) is too complex to derive closed form expressions for the minimum mean square error (MMSE) or MAP estimators of the unknown parameters  $\boldsymbol{\alpha}, \boldsymbol{\gamma}$  and  $\mathbf{z}$ <sup>1</sup>. One can think of using the EM algorithm [48] that has received much attention for mixture problems (see [21] and [24] for applications to ultrasound images). However, EM algorithms have many known shortcomings. For instance, they

<sup>1</sup>Note that  $p(\boldsymbol{\theta}, \mathbf{z})$  involves the potential of a Potts Markov field and its intractable partition function  $C(\beta)$  and that  $p(\mathbf{r} | \boldsymbol{\theta}, \mathbf{z})$  is the product of  $N$  indefinite integrals

suffer from *convergence to local maxima or saddle points of the log-likelihood function and sensitivity to starting values* [49, p. 259]. Note that analyzing the concavity properties of the logarithm of (5) is not easy because the  $\alpha$ -Rayleigh distribution does not belong to the exponential family. An interesting alternative is to use a Markov Chain Monte Carlo (MCMC) method generating samples that are asymptotically distributed according to the target distribution (13) [47]. The generated samples are then used to approximate the Bayesian estimators. This strategy has been used successfully in many image processing applications [50]–[54]. One sampling technique allowing the parameters of ultrasound images to be estimated is studied in the next section.

#### IV. HYBRID GIBBS SAMPLER

This section studies a hybrid Metropolis-within-Gibbs sampler for generating samples that are asymptotically distributed according to (13). The histogram of the generated samples is guaranteed to converge to the posterior (13) [47, p. 269]. One of the most popular methods for generating samples distributed according to a distribution whose pdf or probability masses are known up to a multiplicative constant is the Gibbs sampler. The conventional Gibbs sampler draws samples according to the conditional distributions associated with the distribution of interest [here the posterior (13)]. When a conditional distribution cannot be sampled easily, one can resort to a Metropolis–Hastings (MH) move, which generates samples according to an appropriate proposal and accept or reject these generated samples with a given probability. The resulting sampler is referred to as Metropolis-within-Gibbs sampler (see [47] for more details about MCMC methods). The sampler investigated in this section is based on the conditional distributions  $P[z|\boldsymbol{\alpha}, \boldsymbol{\gamma}, \mathbf{r}]$ ,  $p(\boldsymbol{\alpha}|z, \boldsymbol{\gamma}, \mathbf{r})$ , and  $p(\boldsymbol{\gamma}|z, \boldsymbol{\alpha}, \mathbf{r})$  that are described in the next paragraphs (see also [55, Algor. 1]).

##### A. Conditional Probability $P[z|\boldsymbol{\alpha}, \boldsymbol{\gamma}, \mathbf{r}]$

The label vector  $\mathbf{z}$  can be updated coordinate-by-coordinate using Gibbs moves. More precisely, the conditional probabilities  $P[z_n|\mathbf{z}_{-n}, r_n, \alpha_k, \gamma_k]$  can be computed using Bayes’ rule

$$P[z_n = k|\mathbf{z}_{-n}, r_n, \alpha_k, \gamma_k] \propto p(r_n|z_n = k, \boldsymbol{\alpha}, \boldsymbol{\gamma})p(z_n|\mathbf{z}_{-n}) \quad (14)$$

where  $k = 1, \dots, K$  (it is recalled that  $K$  is the number of classes) and where  $\mathbf{z}_{-n}$  is the vector  $\mathbf{z}$  whose  $n$ th element has been removed. The probability (14) is proportional to

$$\pi_{n,k} \triangleq \exp \left[ \sum_{n' \in \mathcal{V}(n)} \beta \delta(k - z_{n'}) \right] p(r_n|z_n = k, \boldsymbol{\alpha}, \boldsymbol{\gamma}) \quad (15)$$

where  $p(r_n|z_n = k, \boldsymbol{\alpha}, \boldsymbol{\gamma})$  has been defined in (6) and is evaluated using the approximations presented in paragraph Section IV-D. Once all the quantities  $\pi_{n,k}$ ,  $k = 1, \dots, K$ , have

been computed, they are normalized to obtain the posterior probabilities  $\tilde{\pi}_{n,k} \triangleq P[z_n = k|\mathbf{z}_{-n}, r_n, \alpha_k, \gamma_k]$  as follows:

$$\tilde{\pi}_{n,k} = \frac{\pi_{n,k}}{\sum_{k=1}^K \pi_{n,k}}. \quad (16)$$

Note that the posterior probabilities of the label vector  $\mathbf{z}$  in (15) and (16) define an MRF. Finally, samples  $z_n$  are generated by drawing discrete variables in  $\{1, \dots, K\}$  with the respective probabilities  $\{\tilde{\pi}_{n,1}, \dots, \tilde{\pi}_{n,K}\}$ . Because of its large dimension, sampling  $\mathbf{z}$  according to (16) is the most computationally intensive step of the proposed hybrid Gibbs sampler. Therefore it is important to choose an efficient implementation for this step. In this work  $\mathbf{z}$  has been sampled using a parallel chromatic Gibbs sampler [56].

##### B. Conditional Probability Density Function $p(\boldsymbol{\alpha}|\boldsymbol{\gamma}, z, \mathbf{r})$

The probability  $p(\boldsymbol{\alpha}|\boldsymbol{\gamma}, z, \mathbf{r})$  can be expressed as follows:

$$p(\boldsymbol{\alpha}|\boldsymbol{\gamma}, z, \mathbf{r}) \propto p(\mathbf{r}|\boldsymbol{\alpha}, \boldsymbol{\gamma}, z)p(\boldsymbol{\alpha})$$

where  $p(\mathbf{r}|\boldsymbol{\alpha}, \boldsymbol{\gamma}, z)$  is defined in (5) and  $p(\boldsymbol{\alpha}) = \prod_{k=1}^K p(\alpha_k)$ . The generation of samples according to  $p(\boldsymbol{\alpha}|\boldsymbol{\gamma}, z, \mathbf{r})$  is not easy to perform. We propose in this paper to sample  $\boldsymbol{\alpha}$  coordinate-by-coordinate using MH moves. In this work, the proposal distribution is a truncated normal distribution centered on the previous value of the chain with variance  $\sigma_{\alpha,k}^2$

$$\alpha_k^* \sim \mathcal{N}_{(0,2)} \left( \alpha_k^{(t-1)}, \sigma_{\alpha,k}^2 \right) \quad (17)$$

where  $\alpha_k^*$  denotes the proposed value at iteration  $t$  and  $\alpha_k^{(t-1)}$  is the previous state of the chain. The hyperparameters  $\sigma_{\alpha,k}^2$  are adjusted to ensure an acceptance ratio close to 1/3, as recommended in [57, p. 316]. This adjustment is performed dynamically by a feedback loop that increases or decreases  $\sigma_{\alpha,k}^2$  depending  $\alpha_k$  on the acceptance ratio over the last 50 iterations. Note that the proposal (17) results from the so-called random walk MH algorithm [47, p. 245]. Finally, since the prior for  $\alpha_k$  is uniform, the MH acceptance rate of the proposed move can be expressed as follows:

$$\text{ratio} = \min \left\{ 1, \frac{\mathcal{N}_{(0,2)} \left( \alpha_k^{(t-1)} | \alpha_k^*, \sigma_{\alpha,k}^2 \right)}{\mathcal{N}_{(0,2)} \left( \alpha_k^* | \alpha_k^{(t-1)}, \sigma_{\alpha,k}^2 \right)} q_{\alpha_k}^{(t)} \right\} \quad (18)$$

where  $q_{\alpha_k}^{(t)} = \prod_{\{n|z_n=k\}} p_{\alpha\mathcal{R}}(r_n|\alpha_k^*, \gamma_k) / p_{\alpha\mathcal{R}}(r_n|\alpha_k^{(t-1)}, \gamma_k)$  and where the likelihoods  $p_{\alpha\mathcal{R}}(r_n|\alpha_k^*, \gamma_k)$  and  $p_{\alpha\mathcal{R}}(r_n|\alpha_k^{(t-1)}, \gamma_k)$  have been computed using the approximations described in Section IV-D.

##### C. Conditional Probability Density Function $p(\boldsymbol{\gamma}|\boldsymbol{\alpha}, z, \mathbf{r})$

The conditional pdf  $p(\boldsymbol{\gamma}|\boldsymbol{\alpha}, z, \mathbf{r})$  can be expressed as follows:

$$p(\boldsymbol{\gamma}|\boldsymbol{\alpha}, z, \mathbf{r}) \propto p(\mathbf{r}|\boldsymbol{\alpha}, \boldsymbol{\gamma}, z)p(\boldsymbol{\gamma})$$

where  $p(\mathbf{r}|\boldsymbol{\alpha}, \boldsymbol{\gamma}, \mathbf{z})$  is defined in (5) and  $p(\boldsymbol{\gamma}) = \prod_{k=1}^K p(\gamma_k)$ . Again, we propose to sample  $\boldsymbol{\gamma}$  coordinate-by-coordinate by using MH moves. The proposal distribution associated with this move is a truncated normal distribution centered on the previous value of the chain with variance  $\sigma_{\gamma,k}^2$

$$\gamma_k^* \sim \mathcal{N}_{\mathbb{R}^+} \left( \gamma_k^{(t-1)}, \sigma_{\gamma,k}^2 \right) \quad (19)$$

where  $\gamma_k^*$  denotes the proposed value at iteration  $t$ ,  $\gamma_k^{(t-1)}$  is the previous state of the chain and  $\mathcal{N}_{\mathbb{R}^+}$  is the Gaussian distribution truncated on  $\mathbb{R}^+$ . The acceptance ratio for this move is

$$\text{ratio} = \min \left\{ 1, \frac{\mathcal{N}_{\mathbb{R}^+} \left( \gamma_k^{(t-1)} | \gamma_k^*, \sigma_{\gamma,k}^2 \right)}{\mathcal{N}_{\mathbb{R}^+} \left( \gamma_k^* | \gamma_k^{(t-1)}, \sigma_{\gamma,k}^2 \right)} q_{\gamma_k}^{(t)} \right\} \quad (20)$$

where

$$q_{\gamma_k}^{(t)} = \prod_{\{n|z_n=k\}}^N \frac{p_{\alpha\mathcal{R}}(r_n|\alpha_k, \gamma_k^*) p(\gamma_k^*|a_0, b_0)}{p_{\alpha\mathcal{R}}(r_n|\alpha_k, \gamma_k^{(t-1)}) p(\gamma_k^{(t-1)}|a_0, b_0)}$$

and where the prior distribution  $p(\gamma_k|a_0, b_0)$  has been defined in (10). Again, the likelihoods  $p_{\alpha\mathcal{R}}(r_n|\alpha_k, \gamma_k^*)$  and  $p_{\alpha\mathcal{R}}(r_n|\alpha_k, \gamma_k^{(t-1)})$  have been computed using the approximations described in Section IV-D.

In the particular case  $\alpha_k = 2$ , the likelihood simplifies to a Rayleigh distribution for which the prior  $p(\gamma_k) = \mathcal{IG}(a_0, b_0)$  is conjugate. As a result the generation of samples from the posterior  $p(\gamma_k|\alpha_k, \mathbf{z}, \mathbf{r})$  reduces to drawing samples from the following inverse gamma distribution

$$\gamma_k^{(t)} \sim \mathcal{IG} \left( a_0 + \sum_{\{n|z_n=k\}}^N 1, b_0 + \frac{1}{2} \sum_{\{n|z_n=k\}}^N r_n^2 \right) \quad (21)$$

where we recall that  $a_0 = 1$  and  $b_0 = 1$ .

#### D. Approximation of the Likelihood

Evaluating the likelihood function defined in (5) involves the computation of the following indefinite integral

$$\int_0^\infty \lambda \exp[-(\gamma_k \lambda)^{\alpha_k}] J_0(r_n \lambda) d\lambda. \quad (22)$$

In the case where observations are represented using 8-bit precision (i.e., 256-gray levels) the integral can be precomputed for each level and stored in a look-up-table. The data used in this work is represented using 32-bit precision and the integral had to be solved numerically. This computation is time-consuming and is required for every observation and at every step of the sampler. An efficient way to alleviate this computational complexity is to use the following asymptotic expansions [58], [59]

$$p_{\alpha\mathcal{R}}(r_n|\alpha_k, \gamma_k) = \sum_{p=0}^P a_p r_n^{2p+1} + o\left(r_n^{2(P+1)+1}\right) \quad (23)$$

as  $r_n \rightarrow 0$  and

$$p(r_n|\alpha_k, \gamma_k) = \sum_{p=1}^P b_p r_n^{-\alpha_k p - 1} + o\left(r_n^{-\alpha_k(P+1)-1}\right) \quad (24)$$

as  $r_n \rightarrow \infty$ , where the coefficients  $a_p$  and  $b_p$  are

$$a_p = \frac{1}{\alpha_k \gamma_k} \frac{(-1)^p}{(p!)^2 2^{2p}} \Gamma\left(\frac{2p+2}{\alpha_k}\right) \gamma_k^{-2p-1}$$

$$b_p = \frac{(-1)^{p-1} 2^{p\alpha_k+1}}{p! \pi \gamma_k} \Gamma^2\left(\frac{p\alpha_k+2}{2}\right) \sin\left(\frac{p\pi\alpha_k}{2}\right) \gamma_k^{p\alpha_k+1}.$$

The decision between using (23) or (24) for a particular value  $r_n$  has been determined by a threshold which has been computed offline. This threshold and the choice of  $P$  have been studied empirically by comparing (23) and (24) to a numerical solution of the true density (5). Appropriate threshold and  $P$  values have been selected offline for different values of  $\alpha_k$  and stored in a look-up-table that is used by the proposed algorithm. Other considerations regarding the implementation of (23) and (24) have been studied in [58].

## V. EXPERIMENTAL RESULTS

This section presents experimental results conducted on synthetic and real data to assess the performance of the proposed  $\alpha$ -Rayleigh mixture model and the associated Bayesian estimation algorithm. In these experiments the algorithm convergence has been assessed using the ‘‘between-within variance criterion,’’ initially studied by Gelman and Rubin [60] and often used to monitor convergence [61, p. 33]. This criterion requires running  $M$  parallel chains of length  $L$  with different starting values and computing the so-called *potential scale reduction factor* (PSRF) that compares the between-sequence and within-sequence variances [60]. A PSRF close to 1 indicates good convergence of the sampler. In our experiments we have observed PSRF values smaller than 1.01 which confirm the good convergence of the sampler (a PSRF below 1.2 is recommended in [62, p. 332]). These values were computed using  $M = 25$  parallel chains of length  $L = 1000$  whose first 900-steps were discarded.

### A. Synthetic Data

To validate the proposed Bayesian method under controlled ground truth conditions [i.e., known true class labels  $\mathbf{z}$  and statistical parameters  $(\boldsymbol{\alpha}, \boldsymbol{\gamma})$ ], the algorithm described in Section IV was first applied to the synthetic three-component  $\alpha$ -Rayleigh mixture displayed in Fig. 4(a). The parameters associated with the mixture components of the three different 2-D regions are  $\boldsymbol{\alpha} = [1.99, 1.99, 1.8]^T$  and  $\boldsymbol{\gamma} = [1, 5, 10]^T$ . Fig. 4(b) shows the resulting observation vector  $\mathbf{r}$ , which is the only input provided to the algorithm. Note that the different observations are clearly spatially correlated. The proposed Gibbs sampler has been run for this example using a two-dimensional random field with a four-pixel neighborhood structure and a granularity coefficient  $\beta = 1$ . Fig. 5 shows histograms of the parameters generated by the proposed Gibbs sampler. These histograms are in good agreement with the actual values of the different parameters. Moreover, the MMSE estimates and the corresponding standard deviations for the different parameters are reported in Table I. These estimates have been computed from a single Markov chain of 25 000 iterations whose first 100



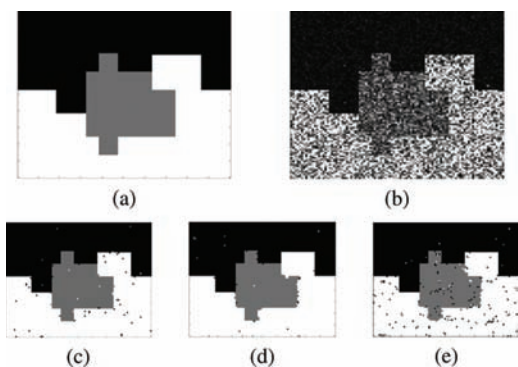


Fig. 4. (a) True labels, (b) observations, MAP label estimates for (c)  $\beta = 1$ , (d)  $\beta = 1.2$ , and (e)  $\beta = 0.8$ .

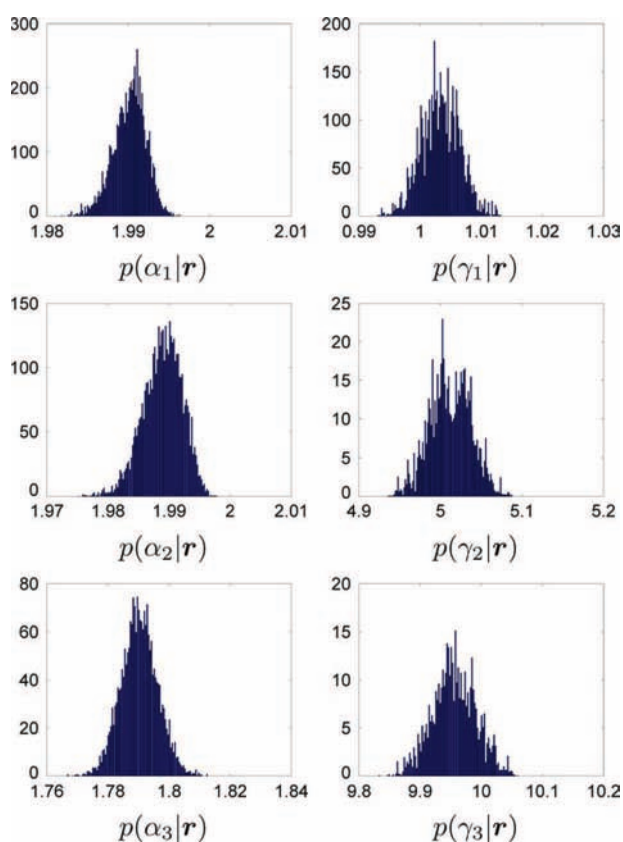


Fig. 5. Histograms of parameters generated using the proposed Gibbs sampler.

iterations (burn-in period) have been removed. The MMSE estimates are clearly in good agreement with the actual values of the  $\alpha$ -Rayleigh mixture components. Fig. 4(c) shows the class labels estimated by the MAP rule applied to the last samples of the Markov chain. The three classes are recovered with a few misclassifications due to the complexity of the problem.

In order to illustrate the effect of the granularity parameter, we have considered other values of the parameter  $\beta$ . Fig. 4(d) and (e) show the class labels obtained with  $\beta = 1.2$  and  $\beta = 0.8$ . We observe that increasing  $\beta$  from 1.0 to 1.2 reduces significantly the number of isolated misclassifications at the expense of increasing errors at the boundaries between the different classes. Decreasing  $\beta$  from 1 to 0.8 increases the number of misclassifications both at the boundaries and within regions.

TABLE I  
PARAMETER ESTIMATION

	true value	MMSE estimates	standard deviation
$\alpha_1$	1.99	1.99	0.002
$\gamma_1$	1.00	1.00	0.003
$\alpha_2$	1.99	1.99	0.003
$\gamma_2$	5.00	5.01	0.025
$\alpha_3$	1.80	1.79	0.006
$\gamma_3$	10.00	9.96	0.036

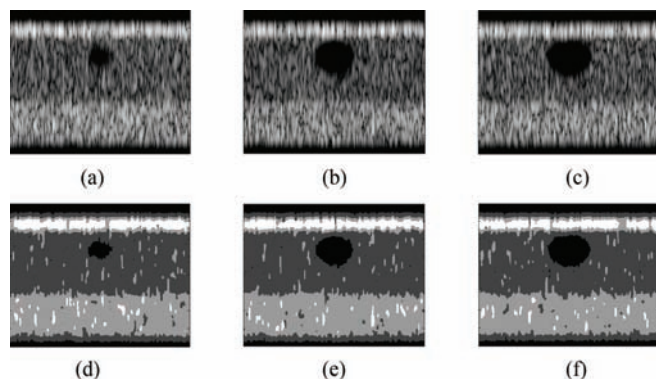


Fig. 6. Simulated (log-compressed) US images of skin layers with an intra-dermic lesion and the corresponding estimated labels. Images (a)–(c) depict three slices of the 30-slice 3-D digital phantom. Images (d)–(f) show the corresponding segmentation results. (a) Phantom (sl. 5/30). (b) Phantom (sl. 10/30). (c) Phantom (sl. 15/30). (d) MAP  $z$  (sl. 5/30). (e) MAP  $z$  (sl. 10/30). (f) MAP  $z$  (sl. 15/30).

### B. Simulated 3-D Ultrasound Image

The synthetic image studied previously is a toy image that differs from a real ultrasound image in many aspects. These aspects include the spatial organization of skin tissue as well as the different physical phenomena intervening in the formation of ultrasound images (i.e., noise, limited spatial resolution, voxel anisotropy, attenuation, etc.). In order to consider a more realistic scenario, the second set of experiments considers a simulated 3-D phantom of skin tissue. This 3-D phantom image has been simulated using a 3-D ultrasound simulator [63], which has been configured with the parameters of the *dermocup* ultrasound system (Atys Medical, France) used in the *in vivo* experiments of Section V-C. Three slices of the 30-slice 3-D phantom are shown in Fig. 6(a)–(c). The size of each slice is  $400 \times 300$  pixels. These images are displayed using logarithmic compression. However the proposed algorithm has been applied to B-mode images in linear scale. The 3-D skin phantom contains three skin layers (epidermis, papillary dermis, and reticular dermis), and one ellipsoidal intra-dermic lesion. Fig. 6(d)–(f) shows the corresponding MAP estimated labels obtained with the proposed method. We observe that the skin layers and the lesion are clearly recovered with a few misclassifications due to the complexity of the problem. The number of classes for this experiment has been set to  $K = 4$  since there are three types of healthy tissue in addition to the lesion. These results were computed using a 3-D MRF with  $\beta = 1.0$  and a single Markov chain of 1000 iterations whose first 900 iterations (burn-in period) have been removed. The

reader is invited to consult the technical report [55] to see segmentation results obtained with other values of  $\beta$ .

### C. Application to Real Data

After validating the proposed Gibbs sampler on synthetic data, this section applies the proposed algorithm to the segmentation of two skin lesions. Experiments were conducted using 3-D high-frequency B-mode ultrasound images of *in vivo* skin tissues. These were acquired with a *dermocup* system (Atys Medical, France), equipped with a single-element focalized 25 MHz wide-band (40%) probe sampled at 100 MHz with a  $53 \mu\text{m}$  mechanic lateral step. The proposed  $\alpha$ -Rayleigh mixture model describes the statistics of envelope (B-mode) ultrasound images without logarithmic compression [28]. Therefore, all experiments have been conducted using this type of data. However, to simplify their visual interpretation, results are displayed using logarithmic compression, which is a standard practice in ultrasound imaging [64]. Note that since  $\alpha$ -Rayleigh envelope signals arise from symmetric  $\alpha$ -stable radio-frequency signals [28] it would be possible to apply the proposed method directly to the radio-frequency ultrasound image by replacing the  $\alpha$ -Rayleigh mixture model (5) by a symmetric  $\alpha$ -stable mixture model [37].

In this work, the number of classes  $K$  is assumed to be known *a priori*. This important parameter is set by the dermatologist who determines visually the number of tissues within the region to be processed. For skin tissues the number of classes depends on the number of layers contained in that region (i.e., epidermis, papillary (upper) dermis, reticular (lower) dermis, hypodermis) in addition to the lesion. When the number of classes is over-estimated, a region is generally divided into two homogeneous parts. For instance, as shown in [55], the segmentation results obtained for  $K = 5$  show an additional class to the core of the lesion, which may correspond to a necrotic tissue. When the number of classes is under estimated, the segmentation results degrade significantly (see [55] for details).

The Potts granularity coefficient  $\beta$  has been chosen heuristically by testing a few values between 0.5 and 1.5. These tests have suggested that segmentation results best agree with expert annotations for  $\beta \in (1, 1.5)$ . Finally,  $\beta$  was set to 1 in order to minimize the risk of over-smoothing the segmentation results, which was the main concern of dermatologists. The reader is invited to consult the technical report [55] to see segmentation results obtained with other values of  $\beta$ . Future work will study the estimation of  $\beta$  jointly with the other unknown parameters of the model, as in [52].

1) *Justification of the  $\alpha$ -Rayleigh Mixture Model:* The  $\alpha$ -Rayleigh mixture model used in this work is based on the assumption that the statistics of single-tissue regions can be well described by an  $\alpha$ -Rayleigh distribution. To support this assumption Fig. 7 compares the histogram obtained from a B-mode ultrasound image of *in vivo* forearm dermis with the corresponding  $\alpha$ -Rayleigh, Nakagami and Gamma distribution fits (additional fits are provided in [28]). To better illustrate fitting at the tails, Fig. 7 displays the probability density functions in logarithmic scale. We observe that the  $\alpha$ -Rayleigh distribution provides the best fit and is the only one to accurately describe the heavy-tail of the histogram.

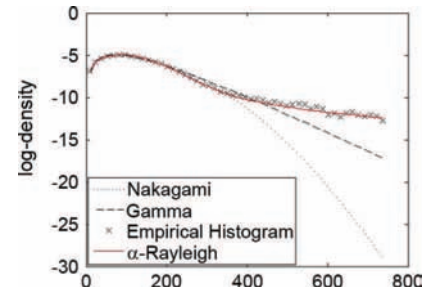


Fig. 7. Comparison of the B-mode histogram obtained from forearm dermis, and the corresponding estimations using the Nakagami, Gamma, and  $\alpha$  Rayleigh distributions. Plots presented in logarithmic scale to illustrate fitting at the tails.

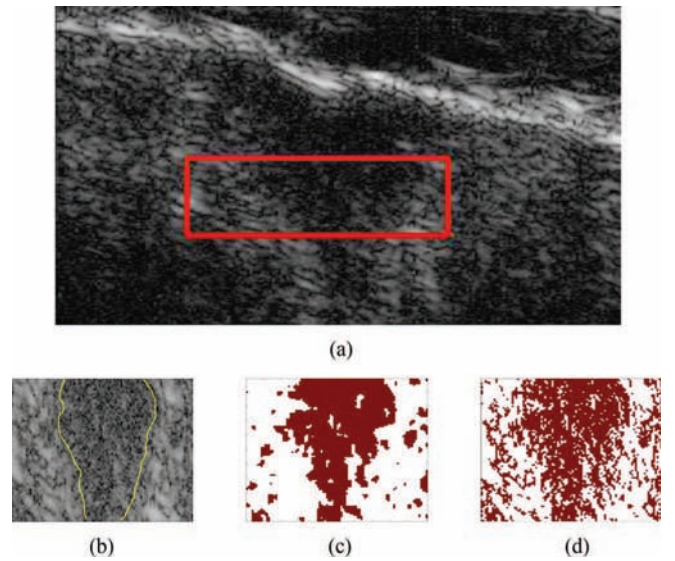


Fig. 8. Log-compressed US images of skin lesion and the corresponding estimated labels (white represents healthy white, red represents lesion) [1]. (a) Dermis view with skin lesion (ROI =  $100 \times 100 \times 3$ ). (b) ROI (slice 2). (c) MRF Labels  $z$ . (d) Independent Labels  $z$ .

2) *Preliminary 2-D and 3-D Experiments:* The two following experiments illustrate the importance of introducing spatial correlation between the mixture components. Fig. 8(a) shows a skin lesion outlined by the red rectangle. This region is displayed with coarse expert annotations (yellow curve) in Fig. 8(b). It should be noted that annotations approximately localize the lesion and do not represent an exact ground truth. The following experiments have been conducted with granularity coefficient  $\beta = 1$  and the number of classes  $K = 2$  since there are only two types of tissue (i.e., lesion and healthy reticular dermis) within the region of interest (ROI). The results have been computed from a single Markov chain of 1000 iterations whose first 900 iterations (burn-in period) have been removed.

First, the proposed Bayesian algorithm was used to label each voxel of the ultrasound image as *healthy* or *lesion* tissue. The estimated labels obtained using a bidimensional random field are displayed in Fig. 8(c). For comparison purposes, Fig. 8(d) shows the estimation results when labels are considered *a priori* independent, as in [1]. Due to the proposed MRF prior for the labels, the spatial correlations between image voxels are clearly recovered with the proposed segmentation procedure.

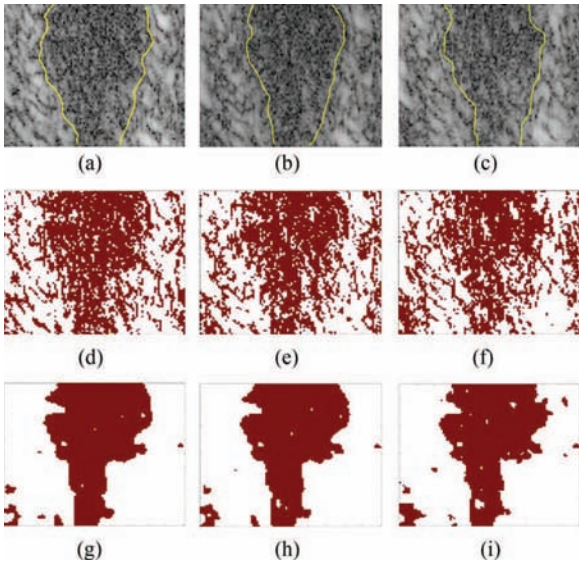


Fig. 9. Log-compressed US images of skin lesion and the corresponding estimated labels (white represents health, red represents lesion). Images (d)–(f) show the results obtained by considering that voxel labels are independent, as in [1]. Images (g)–(i) show the results obtained with the proposed 3-D Markov random field (MRF) method. (a) ROI (slice 1). (b) ROI (slice 2). (c) ROI (slice 3). (d) Ind.  $z$  (slice 1). (e) Ind.  $z$  (slice 2). (f) Ind.  $z$  (slice 3). (g) MRF  $z$  (slice 1). (h) MRF  $z$  (slice 2). (i) MRF  $z$  (slice 3).

In a second experiment the algorithm was applied in three dimensions using a tridimensional random field. Three slices of the 3-D B-mode image associated with the ROI are shown in Fig. 9(a)–(c). Fig. 9(d)–(f) shows the results obtained when labels are considered *a priori* independent, as in [1]. The labels estimated with the proposed 3-D method are displayed in Fig. 9(g)–(i) where healthy voxels are represented in white and lesion voxels in red. The size of the 3-D images is  $100 \times 100 \times 3$  voxels. Computing class label estimates using 1000 iterations of the proposed algorithm required 43.5 s (see Section V-C4 for more details about the computational complexity). We observe that most of the MAP labels are in very good agreement with the expert annotations. The improvement obtained when considering correlations in the third dimension can be assessed by comparing Fig. 8(c) and Fig. 9(h), which have been computed from the same data slice. We observe that using a 3-D MRF reduces significantly the number of misclassifications and improves the agreement with the expert annotations.

3) *Comparison With a State of the Art Method*: The proposed algorithm has been compared with the state of the art method proposed in [25]. This method considers implicitly that the image is a mixture of two Rayleigh components and separates them using an LS algorithm. Comparison has been performed with 2-D and 3-D random fields. The following experiments were conducted with a granularity coefficient  $\beta = 1$  and a number of classes  $K = 4$  since there are three types of healthy tissue within the ROI in addition to the lesion. The results have been computed from a single Markov chain of 1000 iterations whose first 900 iterations (burn-in period) have been removed.

Fig. 10(a) shows a skin lesion contained in the ROI outlined by the red rectangle. This region is displayed with coarse expert annotations in Fig. 10(b). The proposed 2-D Bayesian algorithm was used to label each voxel of the ROI as *healthy* or

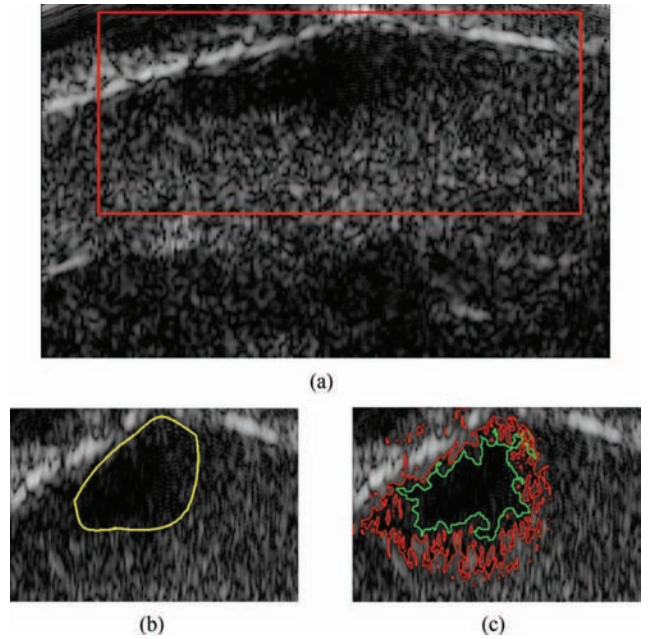


Fig. 10. Log-compressed US images of skin melanoma tumor and the corresponding estimated segmentation contours (green: proposed method, red: [25]).

*lesion* tissue. Then, from the vector of voxels that were labeled as *lesion* we extracted the contour of the largest connected region. The results displayed in Fig. 10(c) show the regular shape of the contour obtained by our method (green curve), whereas the LS method with strong regularization yields a more irregular contour (red curve).

The proposed algorithm was also applied to a 3-D B-mode image using a tridimensional random field. The results for eight slices of the image associated with the ROI depicted in Fig. 10(a) are shown in Fig. 11(a)–(h). The same color code is used for the contours as in the 2-D experiment. The regular shape of the contour obtained by the proposed method is more visible and the recovered lesion fits better the area depicted by the expert. Finally, Fig. 12 shows a 3-D reconstruction of the lesion’s surface (see [55] for more viewpoints). We observe that the tumor has a semi-ellipsoidal shape which is cut at the upper left by the epidermis–dermis junction. The tumor grows from this junction towards the deeper dermis, which is at the lower right.

Finally, it should be noted that in the *in vivo* experiments the proposed algorithm has been applied to ROI, as opposed to entire 3-D images. This has been motivated by the fact that dermatological ultrasound imaging is used to examine specific regions that have been previously identified by the dermatologist. The method presented in this work should be understood in that clinical context and is not intended to be used in unsupervised applications.

4) *Computational Complexity*: Table II provides averaged execution times for 500 iterations of the proposed algorithm for several image sizes in 2-D and 3-D and several numbers of classes. The time required to reach convergence can be calculated by multiplying these values by  $9/5$ , which corresponds to a burn-in period of 900 iterations. These tests have been computed on a workstation equipped with an Intel Core 2 Duo @2.1 GHz

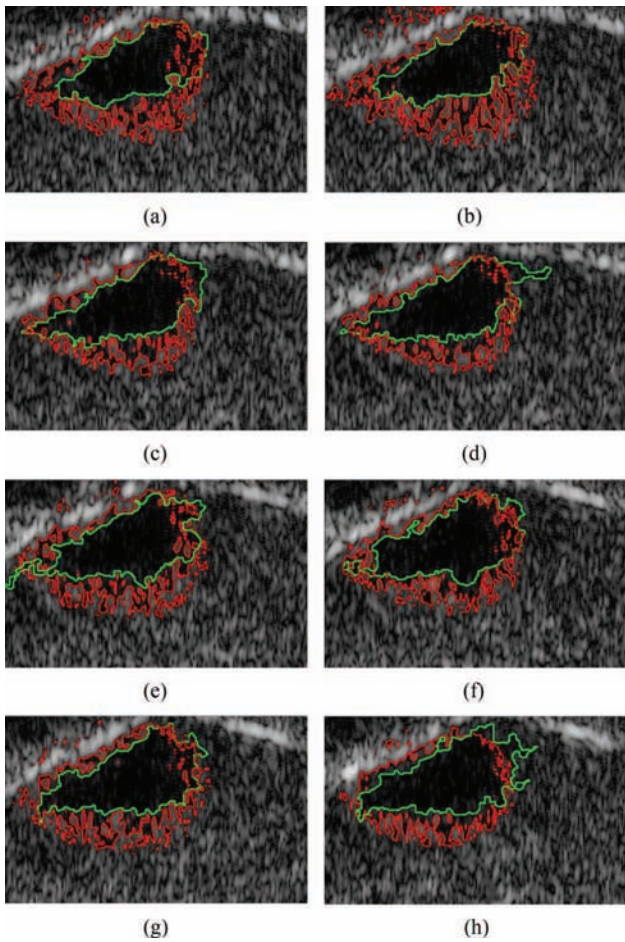


Fig. 11. 3-D segmentation of an eight-slice image. (a) Slice 1. (b) Slice 3. (c) Slice 5. (d) Slice 7. (e) Slice 9. (f) Slice 11. (g) Slice 13. (h) Slice 15.

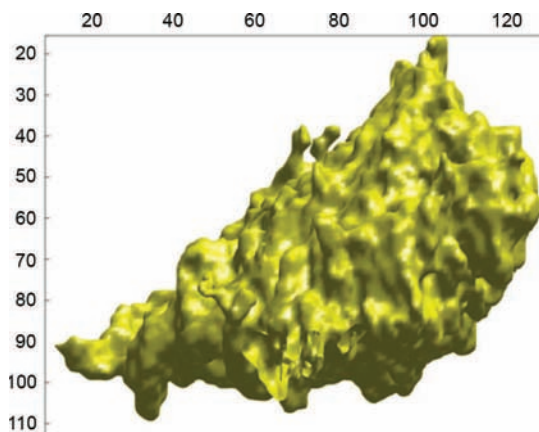


Fig. 12. 3-D reconstruction of the melanoma tumor.

processor, 3 MB L2 and 3 GB of RAM memory. The main loop of the Gibbs sampler has been implemented on MATLAB R2010b (The MathWorks Inc., Natick, MA, 2010). However, C-MEX functions have been used to compute the likelihood and to draw samples of  $z$  from (15). The average execution times of the LS method [25] are provided in [55].

TABLE II  
COMPUTING TIMES (IN SECONDS) OF 500 ITERATIONS FOR  
DIFFERENT IMAGE SIZES AND NUMBER OF CLASSES

	K = 2	K = 4	K = 8	K = 16
$64 \times 64$	4.9	10.2	18.5	35.0
$128 \times 128$	8.1	14.6	27.0	51.7
$256 \times 256$	19.7	36.1	63.5	123.0
$512 \times 512$	73.7	126.0	223.2	427.0
$64 \times 64 \times 16$	20.8	36.6	68.3	129.5
$128 \times 128 \times 16$	75.1	141.5	254.0	524.4
$256 \times 256 \times 16$	317.7	578.1	1060.5	2300.5
$512 \times 512 \times 16$	1175.7	2225.0	4316.8	9600.0

## VI. CONCLUSION

A spatially coherent finite mixture of  $\alpha$ -Rayleigh distributions was proposed to represent the statistics of envelope ultrasound images backscattered from multiple tissues. Spatial correlation was introduced into the model by a Markov random field that promotes dependence between neighbor pixels. Based on the proposed model, a Bayesian segmentation method was derived. Bidimensional and tridimensional implementations of this segmentation method were presented using a Markov chain Monte Carlo algorithm that jointly estimates the unknown parameters of the mixture model and classifies voxels into different tissues. The method was successfully applied to several high-frequency 3-D ultrasound images. Experimental results showed that the proposed technique outperforms a state of the art method in the segmentation of *in vivo* lesions. A tridimensional reconstruction of a melanoma tumor suggested that the resulting segmentations can be used to assess lesion penetration in dermatologic oncology. Future work includes the characterization of the performance of the segmentation algorithm and the study of estimation algorithms for the granularity coefficient defining the Markov random field prior. A comparison with a maximum likelihood estimator followed by median filtering is also considered to be an area of interest for potential future work.

## ACKNOWLEDGMENT

This work was developed as part of the CAMM4D project, supported by the French FUI and the Midi Pyrenees Regional Council. We would like to acknowledge the support of the Hospital of Toulouse, Pierre Fabre Laboratories and Magellium for the ultrasound image acquisition. The authors would particularly like to thank Dr. N. Meyer, Dr. S. Lourari, and J. Georges.

## REFERENCES

- [1] M. A. Pereyra, N. Dobigeon, H. Batatia, and J.-Y. Tourneret, "Labeling skin tissues in ultrasound images using a generalized Rayleigh mixture model," in *Proc. IEEE Int. Conf. Acoust., Speech, Signal Proc. (ICASSP)*, Prague, Czech Republic, May 2011, pp. 729–732.
- [2] M. A. Pereyra, N. Dobigeon, H. Batatia, and J.-Y. Tourneret, "Segmentation of ultrasound images using a spatially coherent generalized Rayleigh mixture model," in *Proc. Eur. Signal Process. Conf. (EUSIPCO)*, Barcelona, Spain, Sep. 2011, pp. 664–668.
- [3] J. Noble and D. Boukerroui, "Ultrasound image segmentation: A survey," *IEEE Trans. Med. Imag.*, vol. 25, no. 8, pp. 987–1010, Aug. 2006.

- [4] A. Belaid, D. Boukerroui, Y. Maingourd, and J.-F. Lerallut, "Phase-based level set segmentation of ultrasound images," *IEEE Trans. Inf. Technol. Biomed.*, vol. 15, no. 1, pp. 138–147, Jan. 2011.
- [5] R. Schneider, D. Perrin, N. Vasilyev, G. Marx, P. de Nido, and R. Howe, "Mitral annulus segmentation from 3-D ultrasound using graph cuts," *IEEE Trans. Med. Imag.*, vol. 29, no. 9, pp. 1676–1687, Sep. 2010.
- [6] K. Somkantha, N. Theera-Umpon, and S. Auephanwiriyaikul, "Boundary detection in medical images using edge following algorithm based on intensity gradient and texture gradient features," *IEEE Trans. Biomed. Eng.*, vol. 58, no. 3, pp. 567–573, Mar. 2011.
- [7] P. Yan, S. Xu, B. Turkbey, and J. Kruecker, "Adaptively learning local shape statistics for prostate segmentation in ultrasound," *IEEE Trans. Biomed. Eng.*, vol. 58, no. 3, pp. 633–641, Mar. 2011.
- [8] G. Unal, S. Bucher, S. Carlier, G. Slabaugh, T. Fang, and K. Tanaka, "Shape-driven segmentation of the arterial wall in intravascular ultrasound images," *IEEE Trans. Inf. Technol. Biomed.*, vol. 12, no. 3, pp. 335–347, May 2008.
- [9] G. Carneiro, B. Georgescu, S. Good, and D. Comaniciu, "Detection and measurement of fetal anatomies from ultrasound images using a constrained probabilistic boosting tree," *IEEE Trans. Med. Imag.*, vol. 27, no. 9, pp. 1342–1355, Sep. 2008.
- [10] P. Paramanathan and R. Uthayakumar, "Tumor growth in the fractal space-time with temporal density," in *Control, Computation and Information Systems, ser. Communications in Computer and Information Science*. Berlin, Germany: Springer, 2011, vol. 140, pp. 166–173.
- [11] K. Horsch, M. L. Giger, L. A. Venta, and C. J. Vyborny, "Automatic segmentation of breast lesions on ultrasound," *Med. Phys.*, vol. 28, no. 8, pp. 1652–1659, 2001.
- [12] I.-S. Jung, D. Thapa, and G.-N. Wang, "Automatic segmentation and diagnosis of breast lesions using morphology method based on ultrasound," in *Fuzzy Systems and Knowledge Discovery*, L. Wang and Y. Jin, Eds. Berlin, Germany: Springer, 2005, vol. 3614, Lecture Notes in Computer Science, pp. 491–491.
- [13] A. Madabhushi and D. Metaxas, "Combining low-, high-level and empirical domain knowledge for automated segmentation of ultrasonic breast lesions," *IEEE Trans. Med. Imag.*, vol. 22, no. 2, pp. 155–169, Feb. 2003.
- [14] Y.-L. Huang and D.-R. Chen, "Watershed segmentation for breast tumor in 2-d sonography," *Ultrasound Med. Biol.*, vol. 30, no. 5, pp. 625–632, 2004.
- [15] X. Guofang, M. Brady, J. Noble, and Z. Yongyue, "Segmentation of ultrasound B-mode images with intensity inhomogeneity correction," *IEEE Trans. Med. Imag.*, vol. 21, no. 1, pp. 48–57, Jan. 2002.
- [16] D. Boukerroui, A. Baskurt, J. Noble, and O. Basset, "Segmentation of ultrasound images-multiresolution 2-D and 3-D algorithm based on global and local statistics," *Pattern Recognit. Lett.*, vol. 24, no. 4–5, pp. 779–790, 2003.
- [17] J. Dias and J. Leitao, "Wall position and thickness estimation from sequences of echocardiographic images," *IEEE Trans. Med. Imag.*, vol. 15, no. 1, pp. 25–38, Feb. 1996.
- [18] R. Wagner, S. Smith, J. Sandrik, and H. Lopez, "Statistics of speckle in ultrasound B-scans," *IEEE Trans. Sonics Ultrason.*, vol. 30, no. 3, pp. 156–163, May 1983.
- [19] E. Brusseau, C. de Korte, F. Mastik, J. Schaar, and A. van der Steen, "Fully automatic luminal contour segmentation in intracoronary ultrasound imaging—a statistical approach," *IEEE Trans. Med. Imag.*, vol. 23, no. 5, pp. 554–566, May 2004.
- [20] C. Chesnaud, P. Refregier, and V. Boulet, "Statistical region snake-based segmentation adapted to different physical noise models," *IEEE Trans. Pattern Anal. Mach. Intell.*, vol. 21, no. 11, pp. 1145–1157, Nov. 1999.
- [21] M. H. R. Cardinal, J. Meunier, G. Soulez, R. L. Maurice, E. Therasse, and G. Cloutier, "Intravascular ultrasound image segmentation: A three-dimensional fast-marching method based on gray level distributions," *IEEE Trans. Med. Imag.*, vol. 25, no. 5, pp. 590–601, May 2006.
- [22] S. Osher and J. A. Sethian, "Fronts propagating with curvature-dependent speed: Algorithms based on Hamilton-Jacobi formulations," *J. Comput. Phys.*, vol. 79, no. 1, pp. 12–49, 1988.
- [23] L. Saroul, O. Bernard, D. Vray, and D. Friboulet, "Prostate segmentation in echographic images: A variational approach using deformable superellipse and Rayleigh distribution," in *Proc. IEEE Int. Symp. Biomed. Imag. (ISBI)*, Paris, France, May 2008, pp. 129–132.
- [24] F. Destrempes, J. Meunier, M. F. Giroux, G. Soulez, and G. Cloutier, "Segmentation in ultrasonic B-mode images of carotid arteries using mixture of Nakagami distributions and stochastic optimization," *IEEE Trans. Med. Imag.*, vol. 28, no. 2, pp. 215–229, Feb. 2009.
- [25] A. Sarti, C. Corsi, E. Mazzini, and C. Lamberti, "Maximum likelihood segmentation of ultrasound images with Rayleigh distribution," *IEEE Trans. Ultrason. Ferroelect. Freq. Contr.*, vol. 52, no. 6, pp. 947–960, Jun. 2005.
- [26] T. Chan and L. Vese, "Active contours without edges," *IEEE Trans. Image Process.*, vol. 10, no. 2, pp. 266–277, Feb. 2001.
- [27] F. Lecellier, J. Fadili, S. Jehan-Besson, G. Aubert, M. Revenu, and E. Saloux, "Region-based active contours with exponential family observations," *J. Math. Imag. Vis.*, vol. 36, pp. 28–45, Jan. 2010.
- [28] M. A. Pereyra and H. Batatia, "Modeling ultrasound echoes in skin tissues using symmetric  $\alpha$ -stable processes," *IEEE Trans. Ultrason. Ferroelect. Freq. Contr.*, vol. 59, no. 1, pp. 60–72, Jan. 2012.
- [29] F. Y. Wu, "The Potts model," *Rev. Mod. Phys.*, vol. 54, no. 1, pp. 235–268, Jan. 1982.
- [30] O. Eches, N. Dobigeon, and J.-Y. Tournet, "Enhancing hyperspectral image unmixing with spatial correlations," *IEEE Trans. Geosci. Remote Sens.*, vol. 49, no. 11, pp. 4239–4247, Nov. 2011.
- [31] D. Van de Sompel and M. Brady, "Simultaneous reconstruction and segmentation algorithm for positron emission tomography and transmission tomography," in *Proc. 5th IEEE Int. Symp. Biomed. Imag.: From Nano to Macro*, Paris, France, May 2008, pp. 1035–1038.
- [32] B. Scherrer, F. Forbes, C. Garbay, and M. Dojat, "Distributed local MRF models for tissue and structure brain segmentation," *IEEE Trans. Med. Imag.*, vol. 28, no. 8, pp. 1278–1295, Aug. 2009.
- [33] L. Risser, J. Idier, P. Ciuciu, and T. Vincent, "Fast bilinear extrapolation of 3-D ising field partition function. Application to fMRI image analysis," in *Proc. ICIP*, Cairo, Egypt, 2009, pp. 833–836.
- [34] J. Marroquin, E. Santana, and S. Botello, "Hidden Markov measure field models for image segmentation," *IEEE Trans. Patt. Anal. Mach. Intell.*, vol. 25, no. 11, pp. 1380–1387, Nov. 2003.
- [35] M. Woolrich, T. Behrens, C. Beckmann, and S. Smith, "Mixture models with adaptive spatial regularization for segmentation with an application to fMRI data," *IEEE Trans. Med. Imag.*, vol. 24, no. 1, pp. 1–11, Jan. 2005.
- [36] P. Morse and K. Ingard, *Theoretical Acoustics*. Princeton, NJ: Princeton Univ. Press, 1987.
- [37] D. Salas-Gonzalez, E. E. Kuruoglu, and D. P. Ruiz, "Finite mixture of  $\alpha$ -stable distributions," *Digit. Signal Process.*, vol. 19, pp. 250–264, Mar. 2009.
- [38] E. E. Kuruoglu and J. Zerubia, "Modeling SAR images with a generalization of the Rayleigh distribution," *IEEE Trans. Image Process.*, vol. 13, no. 4, pp. 527–533, Apr. 2004.
- [39] A. Achim, E. E. Kuruoglu, and J. Zerubia, "SAR image filtering based on the heavy-tailed Rayleigh model," *IEEE Trans. Image Process.*, vol. 15, no. 9, pp. 2686–2693, Sep. 2006.
- [40] S. Geman and D. Geman, "Stochastic relaxation, Gibbs distributions, and the Bayesian restoration of images," *IEEE Trans. Patt. Anal. Mach. Intell.*, vol. 6, no. 6, pp. 721–741, Nov. 1984.
- [41] J. Besag, "Spatial interaction and the statistical analysis of lattice systems," *J. Roy. Stat. Soc.*, vol. 36, no. 2, pp. 192–236, 1974.
- [42] R. Kindermann and J. L. Snell, *Markov random fields and their applications*. Providence, RI: Amer. Math. Soc, 1980.
- [43] Z. Zhou, R. Leahy, and J. Qi, "Approximate maximum likelihood hyperparameter estimation for Gibbs prior," *IEEE Trans. Image Process.*, vol. 6, no. 6, pp. 844–861, Jun. 1997.
- [44] X. Descombes, R. Morris, J. Zerubia, and M. Berthod, "Estimation of Markov random field prior parameters using Markov chain Monte Carlo maximum likelihood," *IEEE Trans. Image Process.*, vol. 8, no. 7, pp. 945–963, Jun. 1999.
- [45] J. Moller, A. N. Pettitt, R. Reeves, and K. K. Berthelsen, "An efficient Markov chain Monte Carlo method for distributions with intractable normalising constants," *Biometrika*, vol. 93, no. 2, pp. 451–458, Jun. 2006.
- [46] C. McGrory, D. Titterton, R. Reeves, and A. Pettitt, "Variational Bayes for estimating the parameters of a hidden Potts model," *Stat. Comput.*, vol. 19, pp. 329–340, 2009.
- [47] C. P. Robert and G. Casella, *Monte Carlo Statistical Methods*. New York: Springer-Verlag, 1999.
- [48] A. P. Dempster, N. M. Laird, and D. B. Rubin, "Maximum likelihood from incomplete data via the EM algorithm," *J. R. Stat. Soc.*, vol. 39, no. 1, pp. 1–38, 1977.
- [49] J. Diebolt and E. H. S. Ip, "Stochastic EM: Method and application," in *Markov Chain Monte Carlo in Practice*, W. R. Gilks, S. Richardson, and D. J. Spiegelhalter, Eds. London, U.K.: Chapman & Hall, 1996.
- [50] N. Dobigeon and J.-Y. Tournet, "Bayesian orthogonal component analysis for sparse representation," *IEEE Trans. Signal Process.*, vol. 58, no. 5, pp. 2675–2685, May 2010.

- [51] N. Dobigeon, A. Hero, and J.-Y. Tournet, "Hierarchical Bayesian sparse image reconstruction with application to MRFM," *IEEE Trans. Image Process.*, vol. 18, no. 9, pp. 2059–2070, Sep. 2009.
- [52] T. Vincent, L. Risser, and P. Ciucu, "Spatially adaptive mixture modeling for analysis of fMRI time series," *IEEE Trans. Med. Imag.*, vol. 29, no. 4, pp. 1059–1074, Apr. 2010.
- [53] K. Kayabol, E. Kuruoglu, and B. Sankur, "Bayesian separation of images modeled with MRFs using MCMC," *IEEE Trans. Image Process.*, vol. 18, no. 5, pp. 982–994, May 2009.
- [54] M. Mignotte, "Image denoising by averaging of piecewise constant simulations of image partitions," *IEEE Trans. Image Process.*, vol. 16, no. 2, pp. 523–533, Feb. 2007.
- [55] M. Pereyra, N. Dobigeon, H. Batatia, and J.-Y. Tournet, Segmentation of skin lesions in 2-D and 3-D ultrasound images using a spatially coherent generalized Rayleigh mixture model Univ. Toulouse, France, IRIT/INP-ENSEEIH, 2011 [Online]. Available: [http://pereyra.perso.enseeiht.fr/pdf/Pereyra\\_TMI\\_TR\\_2011.pdf](http://pereyra.perso.enseeiht.fr/pdf/Pereyra_TMI_TR_2011.pdf)
- [56] J. Gonzalez, Y. Low, A. Gretton, and C. Guestrin, "Parallel Gibbs sampling: From colored fields to thin junction trees," in *Proc. Artif. Intell. Stat. (AISTATS)*, Ft. Lauderdale, FL, May 2011.
- [57] G. O. Roberts, "Markov chain concepts related to sampling algorithms," in *Markov Chain Monte Carlo in Practice*, W. R. Gilks, S. Richardson, and D. J. Spiegelhalter, Eds. London, U.K.: Chapman Hall, 1996, pp. 259–273.
- [58] Z. Sun and C. Han, "Heavy-tailed Rayleigh distribution: A new tool for the modeling of SAR amplitude images," in *Proc. IEEE Int. Geosci. Remote Sens. Symp.*, Boston, MA, Jul. 2008, vol. 4, pp. 1253–1256.
- [59] C. L. Nikias and M. Shao, *Signal Processing with Alpha-Stable Distribution and Applications*. New York: Wiley, 1995.
- [60] A. Gelman and D. Rubin, "Inference from iterative simulation using multiple sequences," *Stat. Sci.*, vol. 7, no. 4, pp. 457–511, 1992.
- [61] C. P. Robert and S. Richardson, "Markov chain Monte Carlo methods," in *Discretization and MCMC Convergence Assessment*, C. P. Robert, Ed. New York: Springer Verlag, 1998, pp. 1–25.
- [62] A. Gelman, J. B. Carlin, H. P. Robert, and D. B. Rubin, *Bayesian Data Analysis*. London, U.K.: Chapman Hall, 1995.
- [63] T. Hergum, S. Langeland, E. Remme, and H. Torp, "Fast ultrasound imaging simulation in k-space," *IEEE Trans. Ultrason. Ferroelect. Freq. Contr.*, vol. 56, no. 6, pp. 1159–1167, Jun. 2009.
- [64] T. Szabo, *Diagnostic Ultrasound Imaging*. Boston, MA: Academic, 2004.